Genetic analysis of *Pycr1* and *Pycr2* in mice

Morgane G. Stum,[1] Abigail L. D. Tadenev,[1] Kevin L. Seburn,[1] Kathy E. Miers,[1] Pak P. Poon,[2] Christopher R. McMaster,[2] Carolyn Robinson,[3] Coleen Kane,[1] Kathleen A. Silva,[1] Paul F. Cliften,[4] John P. Sundberg,[1] Laura G. Reinholdt 🄳 ,[1] Simon W. M. John,[1,5,6] and Robert W. Burgess[1,*]

[1]The Jackson Laboratory, Bar Harbor, ME 04609, USA
[2]Department of Pharmacology, Dalhousie University, Halifax, NS B3H 4R2, Canada
[3]Department of Pathology, Dalhousie University, Halifax, NS B3H 4R2, Canada
[4]Department of Genetics, Washington University School of Medicine, St Louis, MO 63110, USA
[5]Department of Ophthalmology, Howard Hughes Medical Institute, New York, NY 10032, USA
[6]Zuckerman Mind Brain Behavior Institute, Columbia University, New York, NY 10032, USA

*Corresponding author: The Jackson Laboratory, 600 Main Street, Bar Harbor, ME 04609, USA. Robert.burgess@jax.org

Abstract

The final step in proline biosynthesis is catalyzed by three pyrroline-5-carboxylate reductases, PYCR1, PYCR2, and PYCR3, which convert pyrroline-5-carboxylate (P5C) to proline. Mutations in human *PYCR1* and *ALDH18A1* (P5C Synthetase) cause Cutis Laxa (CL), whereas mutations in *PYCR2* cause hypomyelinating leukodystrophy 10 (HLD10). Here, we investigated the genetics of *Pycr1 and Pycr2* in mice. A null allele of *Pycr1* did not show integument or CL-related phenotypes. We also studied a novel chemically-induced mutation in *Pycr2*. Mice with recessive loss-of-function mutations in *Pycr2* showed phenotypes consistent with neurological and neuromuscular disorders, including weight loss, kyphosis, and hind-limb clasping. The peripheral nervous system was largely unaffected, with only mild axonal atrophy in peripheral nerves. A severe loss of subcutaneous fat in *Pycr2* mutant mice is reminiscent of a CL-like phenotype, but primary features such as elastin abnormalities were not observed. Aged *Pycr2* mutant mice had reduced white blood cell counts and altered lipid metabolism, suggesting a generalized metabolic disorder. PYCR1 and -2 have similar enzymatic and cellular activities, and consistent with previous studies, both were localized in the mitochondria in fibroblasts. Both *PYCR1* and -*2* were able to complement the loss of Pro3, the yeast enzyme that converts P5C to proline, confirming their activity as P5C reductases. In mice, *Pycr1; Pycr2* double mutants were sub-viable and unhealthy compared to either single mutant, indicating the genes are largely functionally redundant. Proline levels were not reduced, and precursors were not increased in serum from *Pycr2* mutant mice or in lysates from skin fibroblast cultures, but placing *Pycr2* mutant mice on a proline-free diet worsened the phenotype. Thus, *Pycr1* and -*2* have redundant functions in proline biosynthesis, and their loss makes proline a semi-essential amino acid. These findings have implications for understanding the genetics of CL and HLD10, and for modeling these disorders in mice.

Keywords: adipocyte; elastin; skin; metabolism; proline synthesis; cutis laxa; hypomyelinating leukodystrophy

Introduction

PYCR1, PYCR2, and PYCR3 are members of the pyrroline-5-carboxylate reductase family of enzymes. They catalyze the final step of proline synthesis by converting pyrroline-5-carboxylate (P5C) into proline (Figure 1A). PYCR1 and -2 localize to mitochondria, where their P5C substrate is generated from glutamate by P5C Synthase (P5CS), whereas PYCR3 is found in the cytosol and its P5C substrate is generated from ornithine by ornithine aminotransferase (OAT) (De Ingeniis *et al.* 2012). *PYCR1* and *PYCR2* are both associated with human diseases, but with very different clinical manifestations. *PYCR1* mutations cause Cutis Laxa (CL, MIM #612940 and 614438) (Guernsey *et al.* 2009; Reversade *et al.* 2009). In contrast, *PYCR2* mutations cause hypomyelinating leukodystrophy type 10 (HLD10, MIM #616420) (Nakayama *et al.* 2015; Zaki *et al.* 2016). There are no diseases yet associated with *PYCR3*.

CL is a group of human disorders characterized by loose or wrinkly skin, especially in face, hands, feet, and torso. General features of the disease also include small stature and joint laxity with frequent hip dislocations. Other organs can also be involved to varying degrees in CL, and abnormalities have been described in the cardiovascular system (aortic root dilation), the eye (myopia, strabismus, cataract), the central nervous system (mild intellectual disability, and corpus callosum agenesis), bones (kyphosis, scoliosis, osteoporosis, and osteopenia), and lungs (for review, see Morava *et al.* 2009).

The inherited forms of CL are divided into subgroups, according to the mode of inheritance and the gene affected. Mutations in Elastin (*ELN*) (Tassabehji *et al.* 1998; Szabo *et al.* 1999; Zhang *et al.* 1999; Urban *et al.* 2005), Fibulin4 (*FBLN4*) (Hucthagowder *et al.* 2006; Dasouki *et al.* 2007; Hoyer *et al.* 2009; Renard *et al.* 2010) and Fibulin5 (*FBLN5*) (Loeys *et al.* 2002; Markova *et al.* 2003) were
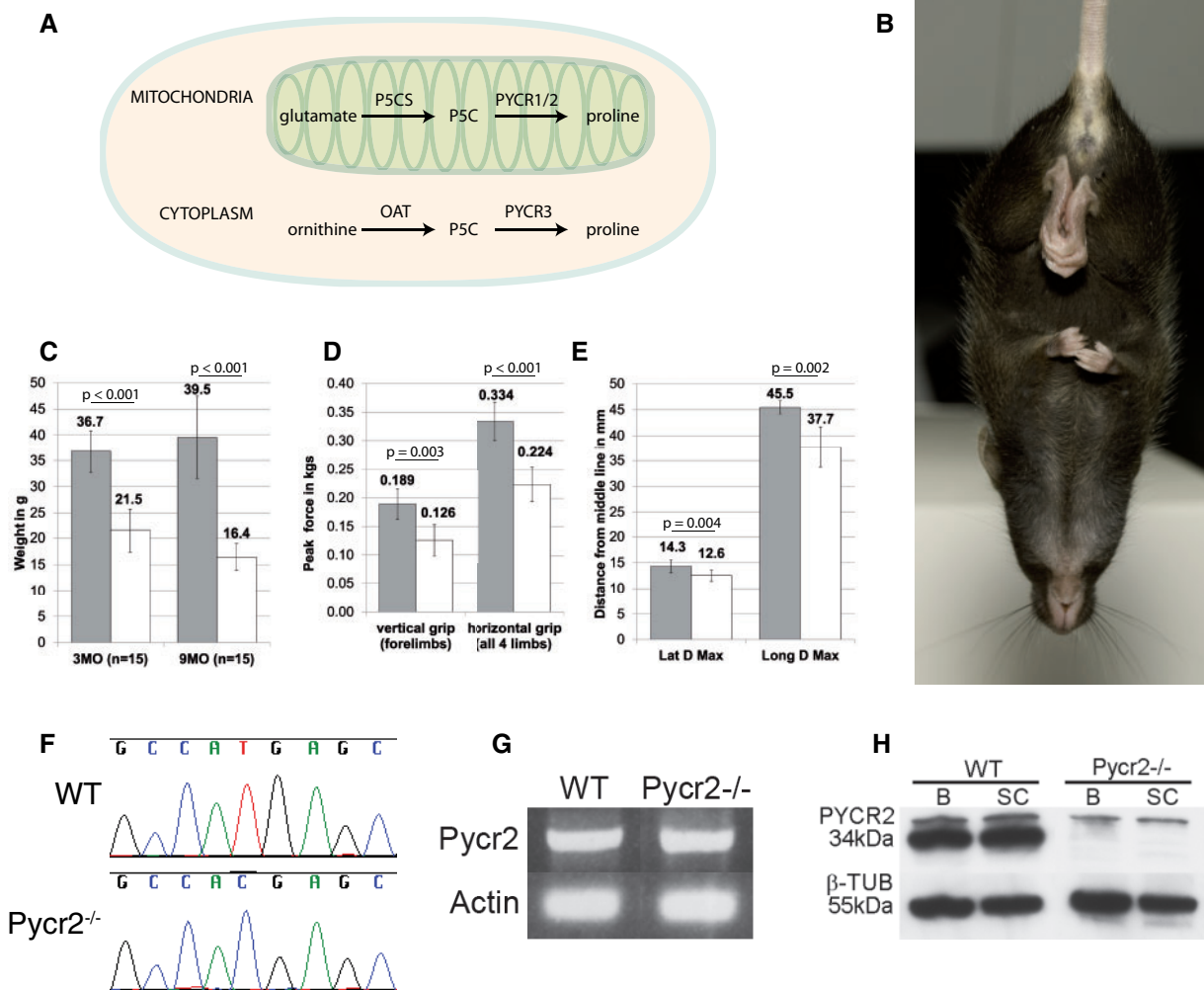
Figure 1 Proline biosynthesis and *Pycr2* mutant mice. (A) In mitochondria, the precursor of proline, pyrroline-5-carboxylate (P5C), is generated from glutamate by pyrroline-5-carboxylate synthase (P5CS, encoded by the gene *Aldh18A1*). P5C is then converted to proline by pyrroline-5-carboxylate reductase-1 or -2 (PYCR1, PYCR2). In the cytosol, P5C is produced from ornithine by ornithine aminotransferase (OAT), and on to proline by pyrroline-5-carboxylate reductase-3 (PYCR3). (B) starting at 3 MO, *Pycr2−/−* mice showed full clasping of limbs. (C–E) *Pycr2−/−* mice show a reduction in weight (C) and grip strength (D), as well as gait abnormalities (E). (WT mice = gray bars, *Pycr2−/−* mice = white bars). (F) Sequencing chromatograms showed a mutation in the pyrroline-5-carboxylate reductase member 2 (*Pycr2*) gene, replacing T by C in the start codon (c.2T>C, p. Met1Thr). (G) RT-PCR analysis revealed normal level of *Pycr2* mRNA in control and mutant mice. (H) Western blots on brain and spinal cord and muscle (B, SC respectively) showed a loss of the 34 kDa PYCR2 specific band. Other nonspecific bands are visible in both mutant and wild-type mice. Bands were cropped and juxtaposed for presentation in G and H.

among the first genes identified as causing CL, implicating the formation and maintenance of elastic fibers in the pathogenesis. More recently, *PYCR1* mutations have been associated with CL (Guernsey *et al.* 2009; Reversade *et al.* 2009). Although rare, numerous patients from dozens of independent families with CL have mutations in *PYCR1* (Kouwenberg *et al.* 2011; Kretz *et al.* 2011; Yildirim *et al.* 2011; Lin *et al.* 2011a; 2011b; Zampatti *et al.* 2012; Dimopoulou *et al.* 2013; Nouri *et al.* 2013; Scherrer *et al.* 2013; Ritelli *et al.* 2017). The fact that *PYCR1* is expressed in skin and bones, the two most affected tissues in CL patients, that elastin is an abundant and very proline-rich protein in these tissues, and that mutations in *ALDH18A1* (encoding P5C Synthetase) are in the same biochemical pathway and also cause CL in patients (Baumgartner *et al.* 2000; Bicknell *et al.* 2008; Skidmore *et al.* 2011) imply that proline biosynthesis also has a critical role in the pathogenesis of CL. In mitochondria, PYCR1 contributes to the cellular response to oxidative stress (Reversade *et al.* 2009); however, its exact role in mitochondrial function and the relationship

between proline synthesis in mitochondria and CL remain to be determined.

Hypomyelinating leukodystrophy 10 (HLD10) has a relatively consistent clinical presentation based on the limited number of cases described (Nakayama *et al.* 2015; Zaki *et al.* 2016; Meng *et al.* 2017; Escande-Beillard *et al.* 2020). Key features include postnatal microcephaly, leukodystrophy, and severe intellectual disability. Patients typically do not survive beyond the first decade of life (Zaki *et al.* 2016). There is some overlap with *PYCR1* phenotypes, including some craniofacial dysmorphology and white matter and intellectual deficits, although these are more severe in *PYCR2*/HLD10 patients (Zaki *et al.* 2016; Meng *et al.* 2017). This may be explained by the higher levels of *PYCR2* than *PYCR1* in brain (Nakayama *et al.* 2015).

Mice lacking *Pycr2* were recently reported (Escande-Beillard *et al.* 2020). Overtly, the mice showed reduced body weight, kyphosis, hind-limb clasping, and ∼one-third died by 35 weeks-of-age. Detailed examination of the brain and cultured neuronal

stem cells showed HLD10-relevant phenotypes, including cell death, axonal dystrophy, and changes in white matter density and oligodendrocyte maturation. Interestingly, the loss of PYCR2 led to an increase in serine hydroxymethyltransferase (SHMT2), which colocalizes in mitochondria and is involved in glycine synthesis. Glycine levels in the brain were indeed elevated in both patients and mice, and knockdown of *Shmt2* in cultured neurons from $Pycr2^{-/-}$ mice largely corrected the *in vitro* phenotypes. Relevant to findings we report below, the authors also assert that proline auxotrophy is not central to the disease mechanism, because circulating proline levels are not different in HLD10 patients or $Pycr2^{-/-}$ mice, and because cultured $Pycr2^{-/-}$ neuronal stem cells proliferated like wild-type cells in proline-free media. In addition, the authors found that loss of PYCR2 in the brain led to a loss of PYCR1, and vice versa, suggesting that these proteins do not compensate for each other.

Here, we have examined a mouse mutation in *Pycr1* generated by the Knockout Mouse Program (KOMP). The KOMP program reports male-specific phenotypes of impaired glucose tolerance and decreased circulating triglycerides, but no phenotypes directly analogous to cutis laxa (http://www.mousephenotype.org/data/genes/MGI:2384795, Dickinson *et al.* 2016). We also identified a chemically induced mutation in *Pycr2*, which shows overt phenotypes consistent with the previous report. We expand the analysis of the $Pycr2^{-/-}$ mice to include the peripheral nervous system, integument, and skeleton. In addition, by generating double mutant mice, and in yeast complementation studies, we show the *Pycr1* and -2 genes are indeed functionally redundant, with double mutant mice being markedly subviable. We also find that proline in normal mouse dietary chow is able to partially suppress the phenotype of *Pycr2* mutant animals, suggesting some role for proline auxotrophy in the phenotype.

Materials and methods
Mouse husbandry
The *Pycr2* mutant mice used in this study were generated in an ENU mutagenesis program conducted at The Jackson Laboratory, and the mutation was induced in a C57BL/6J background and identified based on its overt phenotype followed by positional cloning and exome sequencing to identify the precise genetic lesion. The official allele designation of the ENU-induced mutation in *Pycr2* described here is $Pycr2^{(m1J)}$. *Pycr1* mutant mice (officially $Pycr1^{tm1(KOMP)Vlcg}$, C57BL/6NTac background) were provided by the KOMP program at The Jackson Laboratory. KOMP strains mentioned for *Pycr2* and *Aldh18a1* are officially $Pycr2^{tm1a(EUCOMM)Wtsi}$ and $Aldh18a1^{tm1a(KOMP)Wtsi}$, respectively. All mice in these studies were produced, bred and housed at The Jackson Laboratory, Bar Harbor, Maine. Mouse rooms are regulated on a 12-hour light/12-hour dark cycle and maintained at an ambient temperature of 21–23°C. Mice of the same sex (4 per cage) were housed in duplex polycarbonate cages (31 × 31 × 214 cm) on pressurized individually ventilated mouse racks (Thoren Caging System) with a high efficiency particulate air-filtered supply and exhaust. Regular monitoring for viruses, bacteria, parasites, and microsporidium showed that the colonies were free of infestation by any known mouse pathogen (http://jaxmice.jax.org/health/a6.pdf). All procedures involving mice were approved by The Jackson Laboratory Animal Care and Use Committee. Mice were allowed *ad libitum* access to acidified, filtered tap water (pH 2.8–3.2), and pellets containing 6% fat, 19.3% protein, 1.53% proline (LabDiet 5K52, PMI Nutritional International).

Diet manipulation
For studies manipulating dietary proline, mice were either fed proline-free diet (Baker AA diet with no added proline, 5BDL from TestDiet) and compared to mice on standard LabDiet 5K52, or provided with supplemental proline mixed into the DietGel 76 A cups (ClearH2O) and compared to mice on DietGel without added proline. Mice on DietGel were not provided chow or water, as DietGel replaces both (76% water and 24% "food," of which 4.7% of the total is protein). DietGel cups are ∼75 grams, and we mixed 1 gram of L-Proline (two 500 mg gel caps, AjiPure pharmaceutical grade L-proline) into each gel cup, for a concentration of ∼13mg proline/gram of DietGel. This supplementation achieves an approximately fivefold increase in dietary proline over unsupplemented DietGel. Cohorts were as follows: For proline supplementation, 9 control mice (4 males, 5 females) and 10 $Pycr2^{-/-}$ mutant mice (4 males, 6 females) were fed control DietGel, and 7 control mice (4 males, 3 females) and 7 $Pycr2^{-/-}$ mice (3 males, 4 females) were fed DietGel with additional proline. For proline deprivation, 11 control mice (8 males, 3 females) and 9 $Pycr2^{-/-}$ mice (5 males, 4 females) were fed standard chow, and 8 control mice (3 males, 5 females) and 8 $Pycr2^{-/-}$ mice (6 males, 2 females) were fed proline-free chow. Our outcome measure, maximum weight gain as a fraction of starting weight, was not sensitive to sex in our control mice on either control diet, or when those cohorts were combined. Therefore, we have pooled the sexes when reporting these results for simplicity.

Physiology and behavior
The Chatillon-Ametek Digital Force Gauge, DFIS 2 (Columbus Instruments) was used to determine the strength exerted by the limbs in response to a constant force. The grip-strength meter is positioned vertically to measure front paw strength. A horizontal grip grid was used to measure the grip strength of all four limbs. Peak force is measured in kg for 5 consecutive trials and an average is calculated for each animal.

Gait analysis was performed as previously described (Wooley *et al.* 2005; 2009). Briefly, mice were placed on a transparent treadmill (Columbus Instruments) and allowed to walk at 16.7 cm/sec for approximately 7 seconds in order to obtain at least 6 strides of good data. The gait was recorded at 100 frames per second with a video camera by Basler Vision Technologies. The camera was mounted at a 90-degree angle to the belt and focused on a mirror at a 45-degree angle to belt. The videos (each video is 795 frames) were then analyzed by Treadscan software (Cleversys Inc.). A series of parameters were measured (TreadScan System Parameters & Measures, Clever Sys, Inc., September 2011). The stance time corresponded to the time elapsed while the foot is in contact with the runway. The swing time was the time elapsed while the foot is in the air. The stride length was the distance between successive touchdowns or plantings of the same foot. The Maximum Lateral Deviation (Lat D Max) was the farthest distance that the foot attained relative to the long body axis (nose to tail axis) during the stance. This is the essentially the farthest the foot got away from the body axis. The Maximum Longitudinal Deviation (Long D Max) was the farthest distance that the foot attained relative to the short body axis (waist axis) during the stance. This is the essentially the farthest the foot got away from the waist. Six mice of each genotype were analyzed at 3 months.

The LUNAR PIXIMUS mouse densitometer, an electrically driven dual-energy X-ray absorptiometry machine, was used to measure skeletal and soft tissue mass, enabling assessment of

skeletal and body composition Mice were anesthetized with 2% tribromoethanol by IP injection and placed on individual plastic trays onto the exposure platform of the PIXIMUS. Single 7 minutes scans were acquired. Three mice of each genotype were scanned at 3 months of age.

MicroCAT II scanner, combined with BioVet gating hardware and v2.0 software (Siemens Medical Solutions, Melvern, Pennsylvania), was used to acquire a large series of two-dimensional X-ray images taken around a single axis of rotation. Mice were induced with 5% isoflurane in oxygen at 0.8 L/min and maintained at 1–1.5% isoflurane throughout image acquisition. To image the bones, an X-ray voltage of 75kvp and a current of 500 uA were used for 1,200 ms. Three hundred and sixty projections were taken over a 360 degrees rotation, at a spatial resolution of 48 μm. Three mice of each genotype were scanned at 3 and 9 months of age.

Electrophysiology

Mice were anesthetized with isoflurane (1–1.5%) and placed on a thermostatically regulated heating pad to maintain normal body temperature. Action potentials were produced by subcutaneous stimulation at the sciatic notch and at the ankle. For recording, a needle electrode (active) was inserted in the center of the paw and a second electrode was placed in the skin between the first and second digits (Occhi *et al.* 2005). Conduction velocity of sciatic axons was calculated by measuring the latency of compound motor action potentials recorded in the muscle of the left rear paw [conduction distance/(proximal latency—distal latency)]. At least 6 mice of each genotype at 3 and 9 months were recorded.

Cell culture

Biopsies were taken from the ventral inside skin, cut in small pieces with a razor blade in a gelatinized 60 × 15mm Nunc dish (Thermo Scientific), and incubated at 37 °C in DMEM (D5671 Sigma) supplemented with 10% Fetal Bovine Serum (14501 F Lonza), 1% Penicillin-Streptomycin (15140-122 Gibco) and 1% GlutaMAX (35050-061 Gibco). After a few days, fibroblasts growing out of the explants were washed in PBS (20012-027 Gibco), treated with 0.05% trypsin-EDTA (25300-054 Gibco) and transferred into a new dish. Media was changed twice a week and cells were split 1:4 when confluent.

Molecular biology

For RNA analysis, brains were dissected from 3-month-old $Pycr2^{-/-}$ and littermate control mice and processed following the Trizol LS Reagent protocol (Invitrogen). cDNA was obtained from 3ug of total RNA using the SuperScript III First-Strand Synthesis System for RT-PCR (Invitrogen). PCRs were then conducted using the following primers: ActinF 5'-CAT TGC TGA CAG GAT GCA GAA-3'; ActinR 5'-GCC ACC GAT CCA CAG AGT-3'; Pycr2F 5'-GAC CCG AAG CAA TAA GGA CA-3'; Pycr2R 5'-TTA AGG GCA GCA GGA GAC AC-3'.

For western blot, tissues (brain, spinal cord, muscle, kidney, heart, pancreas, and liver) were freshly dissected and proteins were extracted in lysis buffer [50 mM EDTA, 30 mM triethanol-amine, 50 mMNaCl, 1% Igepal, complete protease inhibitor cocktail (Roche)] using a Dounce homogenizer. Proteins were then loaded on a 4–12% gradient gel (BioRad) and transferred onto a PVDF membrane (Millipore). The membrane was incubated overnight at 4 °C in 5% milk-TBS-0.1% tween with PYCR1 or PYCR2 antibody (1:1,000, Lifespan Biosciences, RRID: AB_2174882) and beta-tubulin antibody (1:1,000, Sigma Aldrich, RRID: AB_609915), followed by HRP conjugated anti-rabbit or anti-mouse IgG

respectively (1:5,000 PerkinElmer), and revealed on CL-Xposure films (Thermo Scientific). The membrane was stripped with an acidic buffer between antibodies (25 mM glycine, 1% SDS, HCl pH = 2).

Histopathology

Brains, muscles (*gastrocnemius, soleus, tibialis anterior*, and *plantaris*), and skin were freshly dissected and fixed overnight in Bouin's fixative, 10% neutral buffered formalin, or Fekete's acid-alcohol-formalin solution. The samples were embedded in paraffin and sectioned at 6 microns with a microtome. Histologic staining (hematoxylin and eosin, luxol fast blue, cresyl violet, Verhoeff, and Masson's trichrome) were performed using standard protocols. Images were taken using a Nikon Eclipse E600 microscope and Leica FX300 camera.

Hind limb muscles were fixed overnight in 4% paraformaldehyde at 4 °C, embedded in 3% agarose and sectioned longitudinally at 150 microns with a vibratome. Sections were labeled overnight with 2H3 anti-neurofilament and anti-SV2 antibodies (1:500, DHSB), then visualized with A488 conjugated anti-mouse IgG1 and co-labeled with A594 conjugated alpha-bungarotoxin (1:500, Molecular Probes). Sections were then mounted in fluorescent mounting medium (Dako) and visualized under a Leica SP5 confocal microscope.

For acetylcholinesterase staining, small muscles (*extensor digitorum longus* and *soleus*) were fixed overnight in 4% paraformaldehyde, washed and put in saturated sodium sulfate solution overnight, then stained in 0.2 mM ethopropazine, 4 mM acetylthiocholine iodine, 10 mM glycine, 3 mM cupric sulfate and 100 mM sodium acetate at pH = 5.5 for 4 hours. After washing, the staining was revealed in 1.25% sodium sulfide solution for 1 minute, and washed again before mounting.

To measure the internodal length of the sciatic nerves, the nerves were dissected and fixed overnight in 4% paraformaldehyde, then teased on microscope slides and dried overnight at room temperature. After rehydration of the nerve fibers in PBS, the nodes of Ranvier were stained with Phospho-Ezrin/Radixin/Moesin anibody (1:200, Cell Signaling) in 1% bovine serum albumin and 1% triton, washed and revealed with A488 conjugated-anti-rabbit (1:500, Molecular probes). Images were analyzed with ImageJ software. At least 2 mice, with a total of at least 20 internodes, per genotype and age group were analyzed.

Skin morphometrics

A total of 12 six-month-old mice were examined (4 mutant females, 2 wild-type females, 2 mutant males, and 4 wild-type males). Samples of both ventral and dorsal skin were taken from defined locations. Tissues were fixed in 4% paraformaldehyde, processed routinely, sectioned at 6 μm, and stained with hematoxylin and eosin (H&E). The hypodermal fat layer (layer of white fat between the dermis and the paniculus carnosus muscle) was measured using DP70 digital camera on a BH2 Olympus Photomicroscope using DP Controller 3.2.1.276 (Olympus Corp., Tokyo, Japan). Most measurements were made using a 10x objective unless the fat layer was too thin in which case a 25x or 40x objective was used. Each objective was calibrated using a 1 mm etched scale on a microscope slide. Five measurements were made and averaged for each sample from each mouse. Statistical significance was tested using a two-way ANOVA of sex by genotype. No effects of sex were found. The combined measurements of dorsal and ventral samples are reported in Figure 3D. The mice used in this study were the offspring of the mapping cross between C57BL/6J and C3H/HeJ, and thus were predominantly

C57BL/6J, but still contained segregating C3H/HeJ loci. In three of four mutant and one of two control female mice, but none of the male mice, there was a mixed inflammatory cell infiltrate in and around late anagen stage hair follicles, consistent with alopecia areata. However, this is known to be present in the C3H genetic background and did not segregate with the *Pycr2* mutation (Sundberg *et al.* 1994; McElwee *et al.* 1999; King *et al.* 2008).

Electron microscopy

Femoral and sciatic nerves and skin, were dissected and fixed overnight at 4 °C in 2% paraformaldehyde, 2% glutaraldehyde in 0.1 M cacodylate buffer, rinsed in the same buffer and post fixed in 1% osmium tetroxide for 2 hours at room temperature. After washing in cacodylate buffer, tissues were dehydrated in ethanol gradients. Ethanol was then replaced by propylene oxide, and the tissues were then processed and embedded in EMBED 812 resin (Electron Microscopy Sciences) and cured at 70 °C for 24 hours. Semithin (1 μm) sections were cut, baked onto glass slides and stained with toluidine blue for histology. For electron microscopy, 90 nM thin sections were collected on 300 mesh copper grids and stained with uranyl acetate/lead citrate. Grids were then viewed using a JEOL JEM-1230 electron microscope. At least 3 mice of each genotype and each age group were used. A total of around 600 axons were measured for nerve analysis for each genotype. The Kolmogorov-Smirnov (KS) statistic test was used to compare the distributions.

Chemistry work on blood and urine

Mice were anesthetized with isofluorane (1–1.5%) and terminal bleeding was done by intracardial puncture. Whole blood (200 μl) was collected in Microtainer® K2EDTA Tubes (BD Diagnostics), and was analyzed with the Siemens Advia 2120 Hematology Analyzer (Siemens Healthcare Diagnostics Inc.). Blood (300 μl) was also collected in serum separator (SST) microtainers (BD Diagnostics) and centrifuged for 10 minutes at 14,000 RPM. The serum was then analyzed in the Beckman UniCel DxC 600 Pro Chemistry Analyzer (Beckman Coulter) with the following kits: for Glucose: Kit# 442640 (Beckman Coulter), for Cholesterol: Kit# 467825 (Beckman Coulter), for Triglyceride: Kit# 445850 (Beckman Coulter), for HDLD: Kit# 650207 (Beckman Coulter), for BUN: Kit# 442750 (Beckman Coulter), for ALT Kit# 442620 (Beckman Coulter), for T4: Kit# 445995 and for GLDH: Kit# GL442 (Randox).

Urine was collected and analyzed in the Beckman UniCel DxC 600 Synchron Clinical Systems (Beckman Coulter) using the following kits form Beckman Coulter: for microalbumin: kit# 475100; for sodium and potassium: kit#467935. At least 10 mice of each genotype were analyzed at 4 MO.

Mitochondrial activity

Brains were freshly dissected from at least 5 mice per genotype and homogenized in CellLytic MT (Sigma). The samples were centrifuged at 6,000 g for 10 minutes, and the supernatant was used to assess the enzymatic activity, using citrate synthase assay kit#CS0720 (Sigma) and BCA protein assay kit#23225 (Pierce) in 96 well plates. For aconitase dosage, we used a modified version of the SPCITR01 protocol form Sigma. The samples were mixed in the activation buffer containing 500 mM TrisHCl, 50 mM sodium citrate, 10 mM MgCl2, 10 mM NAPD, 1% triton, and 2 U/ml isocitrate dehydrogenase, and the absorbance was measured in a spectrophotometer (SpectraMax 190, Molecular Devices) at 340 nm every minute for 30 minutes at 25 °C in a 96 well plate. The slope was then measured in the linear range of the plot representing the absorbance against time, and used to calculate the enzyme activity in units/μg protein, where one unit converts 1 μm of substrate per minute at pH = 7.4 at 25 °C.

Mass spectrometry

Serum samples, from at least 7 3 MO mice per genotype, were diluted 25-fold in 70% acetonitrile + 0.2% acetic acid (v/v) to precipitate proteins. Samples were centrifuged at 21,000 × g at 4 °C for 10 minutes, then the supernatant (250 ul total volume) was transferred to vials containing glass inserts and analyzed on an LC/MS system. Cell pellet samples containing approximately 300,000 fibroblasts from 3 cultures per genotype were resuspended in 300 ul of 100% methanol and homogenized for 1 minute using Fisher Scientific tissue homogenizer equipped with a Kimble glass tissue-grinding pestle. Cell debris was pelleted after samples were centrifuged at 21,000 × g at 4 °C for 10 minutes. Supernatants were transferred to 1.5 ml Eppendorf tubes and samples were lyophilized to dryness under vacuum. Cell extracted samples were resuspended in 250 μl of 70% acetonitrile + 0.2% acetic acid and transferred to vials containing glass inserts. Samples were stored at −80 °C until analyzed by LC/MS.

Samples were analyzed using an Agilent 1260 HPLC in series with an Agilent 6530 accurate mass QTOF instrument. The LC/MS aqueous normal-phase (ANP; - mode) method used to monitor the metabolites was previously reported (Chen *et al.* 2012). Deviations from the method are as follows: the pre-column frit was omitted and the column system consisted of Agilent Zorbax rapid resolution C8 column (2.1 × 30 mm; #873700-936) inline with a Microsolv Cogent Diamond Hydride-4um 100 A column (2.1 × 150 mm; #70000-15 P-2). Negative mode reference ions (68.9956 and 980.0165 m/z) were used to calibrate the mass accuracy of the instrument in real-time. The fragmentor was set to 130. Metabolites were identified using Agilent software suite (Mass Hunter 6.0 and Mass Profiler Professional 12.0). Metabolite identities were determined using the Molecular Feature Extraction (MFE) algorithm and the METLIN database, and then confirmed separately using the Find by Formula (FbF) algorithm. In addition, commercially bought standards of each amino acid/metabolite were analyzed to confirm the observed LC-retention time.

Expression of human PYCR1 and -2 in *Saccharomyces cerevisiae*

To express the human PYCR proteins in the eukaryotic yeast *S. cerevisiae*, the *PYCR* open reading frames were amplified by PCR. *PYCR1* was amplified with primers 5'-CCCAAAGGTTgaattcATGAGCGTGGGCTTCATCGGCGCTG-3' and 5'-CCCGGTTCCCctcgagttaTCAATCCTTGCCCGCTGGGGCCAGG-3' with *PYCR1* cDNA plasmid (cloneID : 5088067, Thermo Scientific) serving as template. *PYCR2* was amplified with primers CCCAAAGGTTgaattcATGAGCGTGGGCTTCATCGGCGCTG-3' and 5'- CCGGTTCCCctcgagttattagtccttcttgcctcccagggccag-3' with the *PYCR2* cDNA plasmid (clone ID: 3919161, Thermo Scientific) serving as template. The amplicons were subcloned downstream of the yeast *GPD1* promoter in vector pPP15:72 to produce pPP17:21-PYCR1 + 1 and pPP17:21-PYCR2 + 1, allowing for constitutive expression of the PYCR proteins in yeast cells. The DNA inserts were sequenced and found to contain no errors.

Plasmid pPP17:21-PYCR1 + 1 and pPP17:21-PYCR2 + 1, and empty vector, were transformed into a yeast strain with an inactivated *PRO3* gene, PPY15:74-W3 (*pro3Δ*::NatMX *leu2–3,112 ura3-1 his3–11,15 trp1–1 ade2-1 can1–100*). The isogenic wild-type yeast strain W303-1a (*PRO3 leu2–3,112 ura3-1 his3–11,15 trp1–1 ade2-1 can1–100*) carrying empty vector pRS316 served as positive

control. Yeast transformants were grown to mid-exponential phase at 30°C in liquid synthetic defined medium (SD; 0.17% yeast nitrogen base without ammonium sulfate and amino acids, 0.1% ammonium sulfate, 2% glucose, 0.004% of leucine, histidine, tryptophan, and 0.002% adenine) supplemented with 0.1% proline. Cells were grown to mid-log phase, cell densities between the separate cell cultures were equilibrated, serially diluted (10-fold dilutions), spotted onto proline-free and 0.1% proline-supplemented solid SD medium (2% agar), and incubated for 3 days at 30°C.

DNA preparation, library construction, and exome sequencing and analysis

Genomic DNA was sonicated to an average size of approximately 200 base pairs. The fragments were blunt ended, "A" tailed and ligated to Illumina sequencing adapters. The ligated fragments were amplified for 7 PCR cycles. Exome targets were enriched with the SureSelect Mouse All Exon kit according to the manufacturer's protocols. Enriched fragments were amplified for 14 cycles with primers that incorporate a unique indexing sequence tag. The resulting library fragments were sequenced from each end (paired-end reads) for 101 bases using an Illumina HiSeq-2000 instrument.

Sequencing reads were aligned to the mouse mm9 reference genome using Novoalign (Novocraft Technologies, Petaling Jaya, Malaysia). PCR duplicates were removed from the alignments with Picard and short variants were called using SAMtools.

Results

Pycr1 mutant mice

Mice lacking *Pycr1* have been characterized by the Knockout Mouse Program (KOMP), an international consortium producing and analyzing mutations in all the genes in the mouse genome. We obtained the $Pycr1^{-/-}$ mice from the KOMP program at JAX, and confirmed that they do not have overt phenotypes or histopathology consistent with CL (https://www.mousephenotype.org/ data/genes/MGI:2384795, and not shown). Broad-based analysis through KOMP revealed male-specific phenotypes in the $Pycr1^{-/-}$ mice, including impaired glucose tolerance and decreased triglyceride levels. No significant differences in skeletal or integument phenotypes were found.

Identification of a *Pycr2* mutation

A *Pycr2* mouse mutation was identified through an ENU mutagenesis program at The Jackson Laboratory. Starting at 3 months of age, affected mice showed clasping of hind limbs and forelimbs when suspended by the tail (Figure 1B). Mutant mice were thinner than their wild-type littermates, weighing 41 and 58% less than controls at 3 months old (3 MO) and 9 months old (9 MO) respectively (t-test $P < 10^{-10}$, Figure 1C). Grip strength was reduced by 33% for both the forelimbs and hind limbs at 3 MO (t-test $P < 0.003$, Figure 1D). Gait analysis at 3 MO revealed no difference in the stance or swing times between wild-type and mutant mice for both front and rear paws (data not shown, $n = 6$, t-test $P > 0.1$), and no difference in the stride length (data not shown, t-test $P > 0.05$). However, a reduction of 12 and 14% of lateral (Lat D Max) and longitudinal (Long D Max) displacement respectively (see methods) was seen on the rear paws of the mutant mice (t-test $P < 0.003$, Figure 1E). It is important to note that gait is influenced by size, and even though mutant mice are thinner than control mice, their skeletal morphometry is normal (see below). To measure the extent to which weight influenced the gait in our

mutant mice, we normalized the displacement distance to the mouse's weight: both lateral (0.36 ± 0.03 vs. 0.52 ± 0.10, t-test $P < 0.004$) and longitudinal (1.14 ± 0.11 vs. 1.55 ± 0.22 t-test $P < 0.003$) displacements were still different between wild-type and mutant mice respectively when related to weight, confirming the tendency of the mutant mice to keep their paws close to their body when walking, an effect that is not wholly explained by reduced body weight.

The ENU mutagenesis was performed in the C57BL/6J inbred genetic background and the mutation was mapped based on the overt phenotypes described above. Breeding suggested a single recessive mutation, with unaffected parents producing approximately 25% affected offspring. Affected (presumed homozygous) mice were crossed with CAST/EiJ mice to generate an obligate heterozygous F1 generation for mapping purposes. The mice were intercrossed to produce an F2 generation. The first mapping with simple sequence length polymorphisms (SSLP *MIT* markers) revealed linkage with Chromosome 1. Further crosses with C3H/ HeJ and fine mapping using additional markers narrowed the interval to 3.2 Mb (from 1:182165749 to 185361875, NCBIm37/mm9). Analysis of exome sequencing results within this interval showed a c.2T>C single nucleotide substitution in the pyrroline-5-carboxylate reductase 2 gene (*Pycr2*) at position 1:182834596 (NCBIm37/ mm9), affecting the start codon p. Met1Thr (Figure 1F). The $T > C$ conversion is consistent with ENU mutagenesis (Barbaric *et al.* 2007), and no other changes were identified within the 3.2 Mb genetic interval. RNA levels were similar between controls and *Pycr2* mutant mice, as shown by RT-PCR on brains from 3 MO mice (Figure 1G). Western blots using an anti-PYCR2 antibody on different tissues from 3 MO mice revealed a loss of the 34 kDa protein in the mutant compared to the control (Figure 1H), confirming the deleterious impact of the mutation. These mice are officially designated as $Pycr2^{(m1J)}$, but are referred to as $Pycr2^{-/-}$ hereafter for brevity. The findings presented here are highly consistent with the characterization of a *Pycr2* null strain analyzed by the KOMP project (https://www.mousephenotype.org/data/ genes/MGI:1277956), and with a recent publication (Escande-Beillard *et al.* 2020).

Neurological assessment of $Pycr2^{-/-}$ mice

Leg clasping phenotype is often indicative of peripheral nervous system abnormalities. We, therefore, examined anatomy and function in the nervous system. Histologic staining on brain sections from 3 to 9 MO mice showed no gross structural changes (not shown). Hind limb muscles appeared normal, with no sign of atrophy or denervation seen by H&E staining (Figure 2, A and B). Hind limb muscles from 9 MO mutants weighed less than control muscles, but there was an increase in the muscle weight to body weight ratio (Figure 2C, t-test $P < 0.02$), indicating that the weight loss seen in $Pycr2^{-/-}$ mice was not due to selective muscle atrophy. Immunostaining using neurofilament and synaptic vesicle antibodies, combined with alpha-bungarotoxin labeling of post-synaptic acetylcholine receptors, revealed well-innervated pretzel-shaped neuromuscular junctions in both control and mutant mice (not shown). No fragmentation of the postsynaptic acetylcholine receptors or swelling of the nerve was seen. Koelle-Friedenwald staining showed normal acetylcholinesterase activity levels (not shown). Thus, the peripheral neuromuscular system appeared normal in the $Pycr2^{-/-}$ mice.

Peripheral nerves were also examined. To study axonal loss and demyelination, nerves were processed for electron microscopy and semithin sections were stained with toluidine blue. No difference in the number of axons was seen in motor femoral
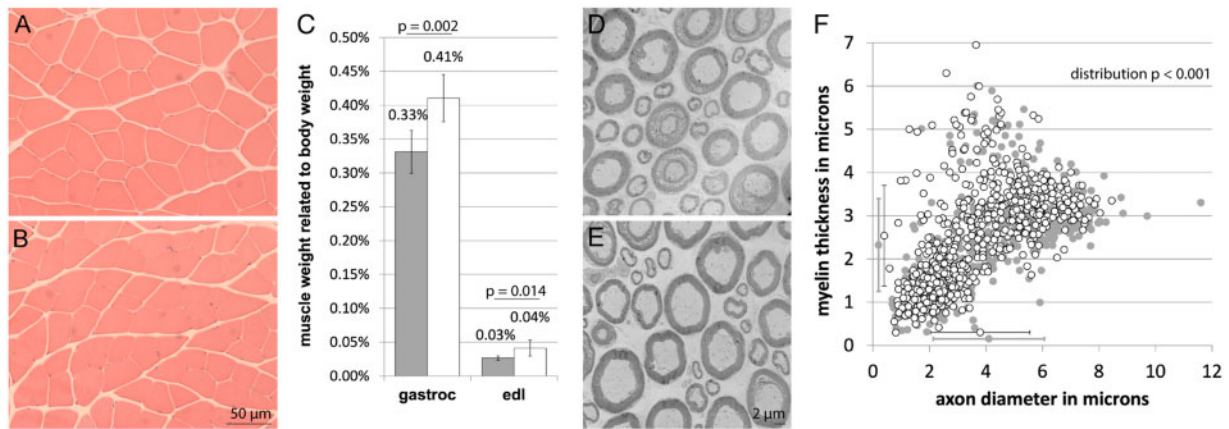
Figure 2 Neuromuscular system. (A and B) Cross sections of the gastrocnemius stained with hematoxylin and eosin showed no abnormalities in *Pycr2$^{-/-}$* mice (B) compared to controls (A) at 3 MO. Scale bar = 50 μm. (C) The muscle weight/body weight ratio was greater in the *Pycr2$^{-/-}$* mice compared to control mice for both *gastrocnemius* (gastroc) and *extensor digitorum longus* (edl). (WT mice = gray bars, *Pycr2$^{-/-}$* mice = white bars). (D and E) Electron microscopy on cross sections of the motor branch of the femoral nerve revealed some smaller axons with thicker myelin in *Pycr2$^{-/-}$* mice (E) compared to control mice (D) at 3 MO. Scale bar = 2 microns. (F) Graphic representation of measurements of myelin thickness and axon diameter (in microns) in the motor branch of the femoral nerve showed a slight but significant shift in *Pycr2$^{-/-}$* mice (open circles) compared to controls (gray circles). Error bars along each axis show the mean ± S. D. of each measure.

nerve (571 ± 50 vs. 552 ± 16 *t*-test *P* > 0.3 at 3 MO, 602 ± 40 vs. 607 ± 43 *t*-test *P* > 0.8 at 9 MO), sensory femoral nerve (789 ± 21 vs. 861 ± 57 *t*-test *P* > 0.1 at 3 MO, 811 ± 69 vs. 832 ± 58 *t*-test *P* > 0.6 at 9 MO), L5 ventral roots (737 ± 268 vs. 647 ± 123 *t*-test *P* > 0.7 at 3 MO) and dorsal roots (2176 ± 770 vs. 1729 ± 497 *t*-test *P* > 0.8 at 3 MO) in wild-type and mutant mice respectively, ruling out axonal loss. However, measurements of axonal diameter and myelin thickness by electron microscopy revealed a difference in the distribution of the G-ratios in the motor branch of the femoral nerve in *Pycr2$^{-/-}$* mice at 3 MO (KS test *P* < 0.001, Figure 2, D and E). Deeper analyses showed that the distribution of both axon diameter (4.10 um ± 1.97 vs. 3.80 um ± 1.75, KS-test *P* < 0.025) and myelin thickness (2.32 um ± 1.07 vs. 2.54 um ± 0.16, KS test *P* < 0.001) were significantly shifted in wild-type versus *Pycr2$^{-/-}$* mice respectively (Figure 2F), revealing a population of smaller atrophic axons with proportionally thicker myelin, a change that is inconsistent with hypomyelination or demyelination in the peripheral nervous system. The distribution of G-ratios in the sciatic nerve was not different between mutant and control mice at 9 MO.

To determine if this shift in axon diameters and myelin thicknesses had functional consequences, we measured the nerve conduction velocities in sciatic axons. No difference was seen between *Pycr2$^{-/-}$* mice and control littermates (40.4 ± 6.8 vs. 37 ± 7.8 *t*-test *P* > 0.4 at 3 MO, 53.8 ± 13.3 vs. 48.7 ± 7.1 at 9 MO *t*-test *P* > 0.2 in wild-type and mutant mice, respectively). To check for a possible adaptive mechanism, we measured the distance between nodes of Ranvier visualized by Phospho-Ezrin/Radixin/Moesin immunostaining in the sciatic nerve. The internodal length was similar between control and *Pycr2$^{-/-}$* mice (559 ± 33um vs. 477 ± 45um *t*-test *P* > 0.1 at 3 MO, 499 ± 14um vs. 600 ± 36um *t*-test *P* > 0.6 at 9 MO). Thus, despite the overt neurological symptom of limb clasping, the *Pycr2$^{-/-}$* mice showed only mild axonal atrophy in the peripheral nervous system, with no other obvious anatomical or functional defects.

Pycr2$^{-/-}$ mice show loss of hypodermal fat

Since patients with *PYCR1* mutations show CL and hyperextensibility of joints (hip dislocation), we also examined related phenotypes in *Pycr2$^{-/-}$* mice. Analysis of the body composition through

Dual Energy X-ray Absorptiometry (DEXA) showed a 53% loss of total body fat (24.6 ± 3.9 vs. 11.6 ± 0.3% of fat in controls vs. *Pycr2$^{-/-}$* respectively, *t*-test *P* < 0.005). Consistent with this, H&E staining on vertical sections of skin revealed a loss of the hypodermal fat layer in *Pycr2$^{-/-}$* mice compared to littermate control mice (Figure 3). The thickness of the hypodermal fat layer changes dramatically with the normal hair cycle in the mouse (Chase 1955; Sundberg and Silva 2012). When the hair cycle was matched, there was a decrease in the thickness of the hypodermal fat layer in mutant mice. (Figure 3, A–D). White fat was mixed with smaller adipocytes that contained relatively uniformly sized clear vacuoles in the mutant mice (Figure 3, B and C). At all phases of the hair cycle, the hypodermal fat layer was reduced in *Pycr2$^{-/-}$* mice compared to littermate controls (362.1 ± 188 vs. 74.4 ± 69 μm in dorsal skin of controls vs. *Pycr2$^{-/-}$* respectively, *P* = 0.007 and 329.1 ± 128 vs. 74.7 ± 57 μm in ventral skin of controls vs. *Pycr2$^{-/-}$* respectively, *P* = 0.004) (Figure 3D). In addition to the reduced hypodermal fat layer, we also specifically examined collagen and elastin in the skin, as elastin defects are central to CL. Qualitatively, the skin was thin, but not easily stretched. Collagen and elastin were present in the dorsal skin dermis in normal proportion and organization, as shown by histologic staining and electron microscopy (Figure 3, E–J). Thus, *Pycr2$^{-/-}$* mice do not have an obvious skin connective tissue or elastin phenotype.

Pycr2$^{-/-}$ have kyphosis, but normal bones and joints

We also examined the skeleton for bone abnormalities and signs of joint laxity. The bone mineral density (0.055 ± 0.004g/cm^2 vs. 0.052 ± 0.003 g/cm^2 *t*-test *P* > 0.4) and the bone mineral content (0.514 ± 0.032 g/cm^2 vs. 0.556 ± 0.067g/cm^2 *t*-test *P* > 0.3) were not different between control and mutant mice respectively. 3D-X-rays of the hips at 3 MO did not show any deformation of the ischium or the femoral head (Supplementary Figure 1). In order to quantify any hip dysplasia, we then measured the acetabular depth-to-width ratio (hip socket), defined by the ratio of the distance to the deepest point of the acetabulum and the perpendicular distance between the upper and lower margin of the acetabulum. No difference was seen between control and
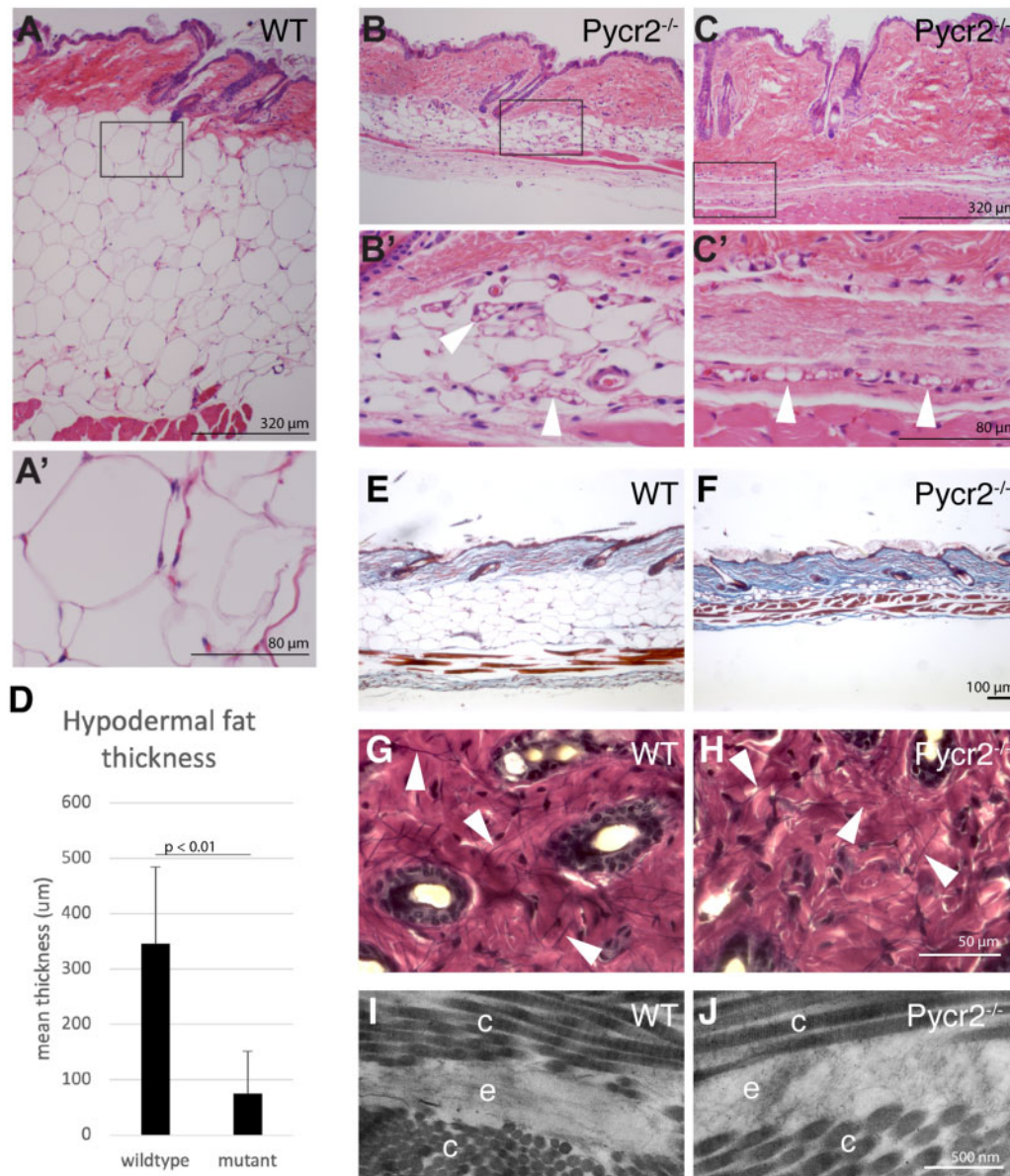
Figure 3 Skin phenotypes in *Pycr2$^{-/-}$* mice. (A) Control mice have a thick hypodermal fat layer. The adipocytes contain one large clear vacuole of lipid, which compresses the nucleus to the side (A'). (B and C) By contrast *Pycr2$^{-/-}$* mice have greatly reduced hypodermal fat regardless of stage of the hair cycle. Of the adipocytes that are present, some have multiple small clear vacuoles, but these make up all that are present in some samples (arrowheads, B', C'). D() On average, the thickness of the hypodermal fat (in µm) was reduced in *Pycr2$^{-/-}$* mutant mice. ($P < 0.01$). Scale bars are 320 µm in low magnification images and 80 µm in high magnification images. (E and F) Trichrome (Masson's) staining on skin cross sections of 3 MO control (E) and *Pycr2$^{-/-}$* (F) mice revealed that collagen was present (blue) in mutant mice. Scale bar = 100um. (G and H) "*en face*" skin sections stained with Verhoeff demonstrated that elastin fibers (dark purple lines, a few examples pointed by arrowheads) are present is the wild-type (G) and the *Pycr2$^{-/-}$* mutant (H) mouse skin at 3 MO. Scale bar = 50um. (I and J) Ultrastructure of skin sections at 3 MO revealed collagen (c) and elastin (e) in normal quantity and organization in control (I) and mutant mice (J). Scale bar = 500 nm.

Pycr2$^{-/-}$ mice (0.64 ± 0.01 vs. 0.61 ± 0.05 respectively, *t*-test $P > 0.4$), indicating that the *Pycr2$^{-/-}$* mice did not suffer from chronic hip dysplasia. However, X-rays at 9 MO revealed spine deformation (kyphosis) in the mutant mice (Supplementary Figure 1), consistent with previous studies (Escande-Beillard *et al.* 2020). To quantify the extent of the kyphosis, we measured the angles that the spine forms between the cervical and thoracic regions, and between the thoracic and the lumbar regions. The angles of the spine curvature were decreased to 55% and 80% of the control values at the neck and the thorax regions respectively in the *Pycr2$^{-/-}$* mutants ($99.8 \pm 19.9°$ vs. $54.3 \pm 15.0°$ *t*-test $P < 0.04$ at the neck; $113.7 \pm 8.9°$ vs. $91.4 \pm 3.4°$ *t*-test $P < 0.02$ at the thorax,

in control and mutant mice, respectively). This condition was not observed at 3 MO, indicating that it is progressive with age. Kyphosis is often associated with hypotonia and loss of strength in postural muscles that keep the spine straight.

Pycr2$^{-/-}$ metabolic studies

As PYCR1 and -2 are reported to be mitochondrial enzymes (Reversade *et al.* 2009; De Ingeniis *et al.* 2012), we verified the localization of PYCR2 in skin fibroblasts *in vitro*, by co-labeling with a PYCR2 antibody and Mitotracker (Figure 4A). While PYCR2 labeling perfectly co-localized with the mitochondrial network in the wild-type cell lines, we observed a loss of this
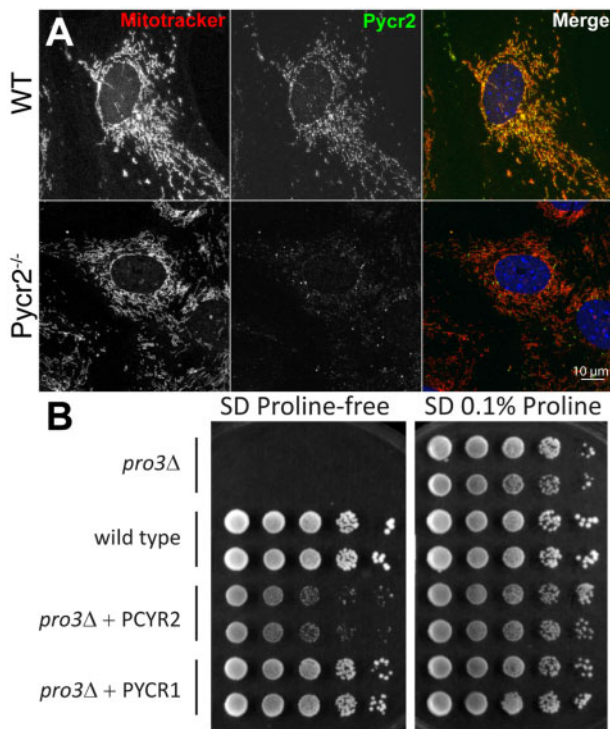
Figure 4 PYCR2 mitochondrial localization in cells and rescue in yeast. (A) Immunostaining using DsRed633 Mitotracker and PYCR2 antibody showed a co-localization of PYCR2 with the mitochondrial network in control (top row). In $Pycr2^{-/-}$ mutant cells, PYCR2 was almost completely gone while the mitochondrial network was unaffected (bottom row). Scale bar = 10 um. (B) The yeast *PRO3* gene encodes the sole pyrroline-5-carboxylate reductase in the yeast genome, and inactivation of the *S. cerevisiae PRO3* gene results in proline auxotrophy. Wild-type yeast cells, or yeast cells with an inactivated *PRO3* gene (*pro3Δ*) transformed with a plasmid expressing human PYCR2, PYCR1, or empty vector, were serial diluted onto plates containing 0.1% proline and onto proline-free media. Cells were incubated at 30°C. The inability of *pro3Δ* yeast to grow in the absence of proline is rescued by expression of either human PYCR1 or PYCR2, showing that these genes encode a functional pyrroline-5-carboxylate reductase. Each row represents a separate transformant.

Table 1 Levels of Proline and Proline precursors

	Ornithine	Glutamate	Proline
Serum WT	1.01	2.91	7.66
Serum Pycr2$^{-/-}$	0.99	1.99*	8.53
Cell WT	0	80.47	11.27
Cell Pycr2$^{-/-}$	0	59.22	9.77

The total number of ions expressed in x1E + 6 for ornithine, glutamate, and proline in mouse serum ($n = 7$/genotype) and fibroblasts ($n = 3$/genotype) was measured by mass spectrometry. No difference in those metabolites levels was shown, except for a 32% decrease of glutamate in $Pycr2^{-/-}$ mice serum (*: t-test $P < 0.04$).

immunoreactivity in the mutant cell lines. However, the mitochondrial network was present and unaffected in the mutant cell lines. We then investigated the mitochondrial function by measuring the activity of two enzymes of the Krebs cycle, citrate synthase and aconitase in brain preparations from 3 MO mice. These enzymes were unchanged in activity in the $Pycr2^{-/-}$ mice when compared to controls (92.31 ± 13.31 vs. 101.76 ± 1.60 units/µg protein, t-test $P > 0.5$ for citrate synthase activity; 6.74 ± 0.5 vs. 6.59 ± 0.98 units/µg protein, t-test $P > 0.7$ for aconitase activity, for control and $Pycr2^{-/-}$ mice respectively). Escande-Beillard et al., showed reduced oxygen consumption rate and mitochondrial dysfunction in differentiated oligodendrocytes, but not in neuronal stem cells (Escande-Beillard *et al.* 2020), so a more cell-type-specific analysis may be needed to identify changes in mitochondrial function *in vivo*; however, the loss of PYCR2 protein does not grossly alter the mitochondrial network.

As PYCR is the last enzyme in the synthesis of proline, we investigated whether proline levels were changed in our $Pycr2^{-/-}$ mice. We used mass spectrometry to measure the levels of proline, as well as pyrroline-5-carboxylate (P5C), ornithine, and glutamate, the major precursors and intermediates in the proline synthesis pathway, in the serum of 3 MO mice, and in skin fibroblasts in culture. In the serum, we found a surprising

1.5-fold decrease in the level of glutamate, and no change in levels of proline (Table 1). In the cells, ornithine was not detected, while glutamate, proline, and P5C were similar in control and $Pycr2^{-/-}$ mice. These results showed that proline levels are unchanged both in serum and in cell lysates and are consistent with findings from HLD10 patients and mice (Meng *et al.* 2017; Escande-Beillard *et al.* 2020).

To investigate if the mice suffered from a generalized metabolic condition, blood cells and serum were analyzed at 3 and 9 MO. The hematology and chemistry were normal at 3 MO. However, the number of white blood cells, especially lymphocytes and basophils, was highly reduced in 9 MO $Pycr2^{-/-}$ mice compared to controls (Table 2), indicating that the $Pycr2^{-/-}$ mice were immune-compromised. Serum analysis revealed low potassium levels in $Pycr2^{-/-}$ mice, associated with elevated blood urea nitrogen (BUN), suggesting compromised renal function. Finally, all the lipid levels that we measured, including cholesterol, high-density lipoprotein (HDL) and triglycerides, were decreased in $Pycr2^{-/-}$ mice, also suggesting altered lipid metabolism. In order to further assay the kidney function, we collected and analyzed urine samples of 4 MO mice. The levels of sodium (163.1 ± 37 vs. 195 ± 57.9 mmol/L, t-test $P = 0.15$) and potassium (200.7 ± 33.3 vs. 161.6 ± 69.9 mmol/L, t-test $P = 0.12$) were similar between control and mutant mice respectively. No microalbumin was detected in urine, suggesting that the renal glomeruli were not damaged at this age. However, fat droplets were detected in half of the mutant mice analyzed. Fat droplets occur when the renal tubular epithelial cells absorb lipids while passing through the glomerulus. This result might indicate early onset renal disease.

In light of the absence of changes in proline levels (Table 1), and the normal expansion of neuronal stem cell cultures in proline-free media (Escande-Beillard *et al.* 2020), we wanted to establish if proline synthesis contributes at all to the pathogenic mechanism of *Pycr2* mutations. We first tested the pyrroline-5-carboxylate reductase function of PYCR2 and compared it to PYCR1 in the same system. For this, we used a yeast complementation assay (Figure 4B). The yeast *S. cerevisiae PRO3* gene encodes the sole pyrroline-5-carboxylate reductase present in the yeast genome. Inactivation of the *PRO3* gene in yeast results in proline auxotrophy. Expression of human *PYCR2* rescued the phenotype by allowing for growth of *pro3Δ S. cerevisiae* cells on medium lacking proline, demonstrating that *PYCR2* does encode a functional pyrroline-5-carboxylate reductase. Human *PYCR1* was similarly able to complement the loss of yeast *PRO3*, confirming the enzymatic interchangeability of these enzymes. Interestingly, *PYCR1* appears to have rescued more robustly. This may be consistent with its more efficient enzymatic activity (De Ingeniis *et al.* 2012), or may reflect differences in expression of the two human proteins in yeast.

Table 2 Blood cell counts and clinical blood chemistry

	3MO		9MO	
	Control	Pycr2$^{-/-}$	Control	Pycr2$^{-/-}$
RBC ($\times 10^6$cells/ul)	9.18 ± 0.48	7.80 ± 1.14	8.87 ± 0.56	8.98 ± 0.55
WBC ($\times 10^3$cells/ul)	0.75 ± 0.28	0.70 ± 0.25	2.37 ± 1.24	1.18 ± 0.66
LYMPH ($\times 10^3$cells/ul)	0.43 ± 0.16	0.28 ± 0.22	1.62 ± 0.99	0.51 ± 0.42*
NEUT ($\times 10^2$cells/ul)	2.03 ± 0.57	3.40 ± 2.60	4.94 ± 2.21	4.78 ± 2.47
EOS ($\times 10^2$cells/ul)	1.00 ± 0.73	0.56 ± 0.35	1.70 ± 0.48	1.56 ± 0.51
MONO ($\times 10^1$cells/ul)	1.50 ± 0.58	1.20 ± 0.45	6.60 ± 3.51	2.80 ± 1.64
BASO ($\times 10^1$cells/ul)	1.00 ± 0.00	1.20 ± 0.45	1.20 ± 0.45	0.20 ± 0.45*
Potassium (mmol/l)	4.28 ± 1.09	5.30 ± 0.52	4.75 ± 0.56	4.41 ± 0.90
BUN (mg/dl)	17.75 ± 2.36	21.83 ± 5.42	18.40 ± 4.34	29.50 ± 5.51*
Cholesterol (mg/dl)	80.25 ± 21.44	77.67 ± 24.94	75.20 ± 12.83	43 ± 2.83*
HDL (mg/dl)	73.45 ± 20.33	65.85 ± 19.76	61.76 ± 9.91	35.30 ± 5.66*
Triglycerides (mg/dl)	59.50 ± 19.84	59.17 ± 41.59	113.2 ± 77.9	59.5 ± 7.8

Analysis of blood showed reduced number of white blood cells, particularly lymphocytes and basophils, reduced potassium levels combined with elevated BUN, and decreased levels of HDL and triglycerides in 9 MO Pycr2$^{-/-}$ mice compared to controls. (*: t-test with P < 0.05).

Pycr1 and Pycr2 interact genetically

To explore possible functional redundancy between PYCR1 and PYCR2 suggested by the yeast studies, we used the classic genetic approach of making *Pycr1*$^{-/-}$; *Pycr2*$^{-/-}$ double mutant (DKO) mice. We found that DKO mice were subviable, with only 2 obtained out of a total of 124 pups (expected # = 13 DKO; Chi-squared test P = 0.0013) (Figure 5A). The crosses to produce these mice were done in two ways. First, double heterozygous mice were bred together, such that 1:16 should have been DKO. Of 96 mice recovered, zero were DKO (6 expected, Chi-squared test P = 0.011). We then fixed the *Pycr1* mutation as homozygous and had the *Pycr2* mutation heterozygous. The 28 mice produced in this cross included the 2 DKOs (7 anticipated, Chi-squared test P = 0.03). The only other genotype that was significantly skewed from expected was *Pycr1*$^{-/-}$; *Pycr2*$^{+/+}$, which were over-represented with 24 observed and only 13 expected (Chi-squared test P = 0.0013). This was driven largely by the second cross with *Pycr1*$^{-/-}$ fixed, in which we found 14 *Pycr1*$^{-/-}$; *Pycr2*$^{+/+}$ mice (7 expected). The two surviving double mutants were dramatically smaller than littermates. One died before weaning and was not recovered for analysis. The second was placed on proline-supplemented DietGel 76 A at weaning, but remained smaller than littermates and was euthanized at 12 weeks of age. It would be interesting to examine the phenotypes of double mutant mice, but generating a cohort large enough for meaningful analysis is not practical, and the poor viability, small size, and poor health of the two mice, we did recover clearly indicate a genetic interaction between *Pycr1* and *Pycr2* consistent with functional redundancy, as the combined phenotype is markedly more severe than the additive phenotype of the single mutants.

Diet manipulation

Vertebrates can make proline from various metabolic precursors (Figure 1A), but proline can be considered a conditionally essential amino acid depending on factors such as the bioavailability of these precursors (Reeds 2000). Consistent with compensation and the complicated nature of this pathway, proline levels are not different in serum of *Pycr2* mutant mice or HLD10 patients (Table 1, Meng *et al.* 2017; Escande-Beillard *et al.* 2020). To address the extent to which proline in the diet may correct the phenotype, offering a possible therapeutic strategy, dietary proline was either supplemented or eliminated in an attempt to modulate the phenotype of *Pycr2*$^{-/-}$ mice in separate, controlled experiments. After weaning at 4-weeks-of-age, mice were placed on a
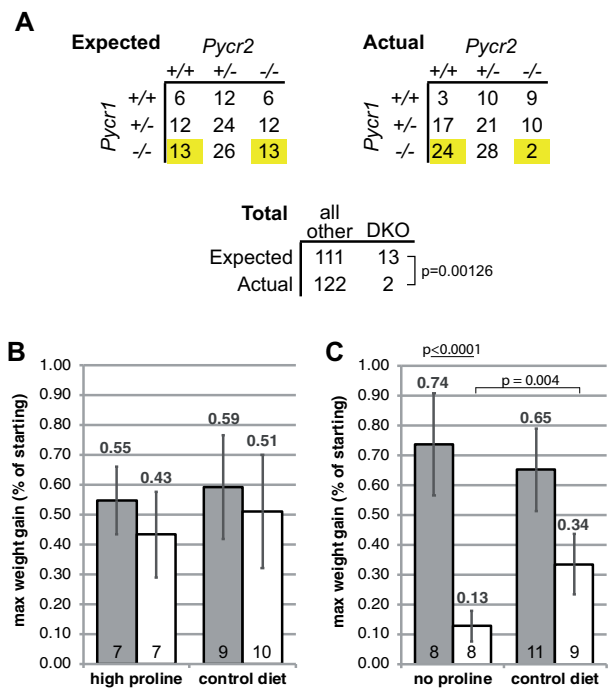
Figure 5 Functional redundancy of *Pycr1* and *Pycr2* and effects of dietary proline. (A) Mice lacking both *Pycr1* and *Pycr2* are subviable, as reflected by the frequency of genotypes observed in two crosses designed to produce double mutant animals. Only two, instead of the anticipated 13, double mutant mice were observed (highlighting), a significant under representation based on Chi-squared testing. The only other genotype that deviated from anticipated was *Pycr1*$^{-/-}$; *Pycr2*$^{+/+}$, which were over represented (24 observed, 13 expected, highlighting). (B and C) *Pycr2*$^{-/-}$ mutants (= white bars) and littermate controls (pooled *Pycr2*$^{+/+}$ and *Pycr2*$^{+/-}$; = gray bars) were fed either a proline-free diet or a diet supplemented with additional proline from 4.5w to 12w of age. Separate cohorts received control diet containing normal proline levels. Weight gain is presented as the maximum net weight gain as a percentage of starting weight. (B) Supplemental proline did not result in greater weight gain over the course of study in *Pycr2*$^{-/-}$ mice. (C) Elimination of proline from the diet of *Pycr2*$^{-/-}$ mice resulted in less weight gain than seen in *Pycr2*$^{-/-}$ mutants fed normal chow. The number of mice in each group is indicated on the graphs.

proline-supplemented or -deficient diet for eight weeks. Both mutant and control mice fed supplemental proline increased body weight, and these results were not different compared to those fed a control diet of unsupplemented DietGel 76 A (Figure 5B).

Proline was mixed into DietGel because of its poor solubility, but this may have confounded this experiment, because the mice ate a surprising amount and mutant mice even on the unsupplemented diet gained more weight than anticipated. We therefore tried the converse experiment of placing mice on a synthetic diet lacking proline. Control mice (pooled $Pycr2^{+/+}$ and $Pycr2^{+/-}$ littermates) on the proline-free diet gained weight similarly to mice on standard chow. However, $Pycr2^{-/-}$ mice that consumed a proline-free diet gained much less weight than control mice on the proline-free diet ($P < 0.0001$), and less weight than mutant mice on standard chow ($P = 0.004$) (Figure 5C). Therefore, removing all proline from the diet worsens the $Pycr2$ mutant phenotype, or phrased more positively, the proline present in standard chow is able to partially suppress the $Pycr2$ mutant phenotype, and mice fed DietGel 76 A with or without added proline had near normal weight gain, suggesting that dietary proline can correct at least the weight loss phenotype.

Discussion

Here, we describe mice carrying a mutation in $Pycr2$, encoding pyrroline-5-carboxylate reductase 2, an enzyme involved in the final step of proline biosynthesis. The protein localizes to mitochondria, is capable of functionally substituting for the single yeast ortholog, *PRO3*, and shows functional redundancy with $Pycr1$ in mice. The $Pycr2$ mutant mice display limb clasping when suspended by the tail, reduced body weight, kyphosis, and a lack of subdermal fat. The basis for these phenotypes is somewhat unclear given that proline levels are normal in both mouse serum samples and lysates of primary skin fibroblasts; however, dietary proline is capable of at least partially suppressing the phenotype. $Pycr1$ mice have no overt phenotypes based on our work, and analysis through the KOMP program did not reveal phenotypes relevant to cutis laxa. Given the association of *PYCR1* with CL and *PYCR2* with HLD10 in humans, we will discuss the implications of our findings for understanding the pathophysiology of these diseases and in comparison to findings in a recent report on $Pycr2^{-/-}$ mice (Escande-Beillard *et al.* 2020).

Overall, our description of $Pycr2^{-/-}$ mice agrees with published data. Most notably, the overt phenotypes of hind-limb clasping, weight loss, and kyphosis are present in our independently identified $Pycr2^{-/-}$ strain. Since neurological and neurodevelopmental phenotypes in the brain and in cell culture were previously characterized in detail (Escande-Beillard *et al.* 2020), we focused on other possible phenotypes. Only mild axon atrophy was identified in the peripheral nervous system, indicating that gait and grip strength abnormalities may be due to CNS problems. Similarly, the skeletal system appeared normal, suggesting that kyphosis is likely due to hypotonia. The mice showed reduced white blood cell counts with age, signs of early stage renal dysfunction, and reduced overall body fat and particularly subdermal fat. Lipids were also altered in clinical blood chemistries. Thus, in addition to previously reported neurological phenotypes, the $Pycr2^{-/-}$ mice appear to have general systemic metabolic problems.

The contribution of proline synthesis, the primary function of the PYCR proteins, to the mouse phenotypes and human CL and HLD10 diseases appears to be complicated. Because proline can normally be made through the pathways in Figure 1A, it is not considered an essential amino acid. However, the loss of sufficient function in these pathways would lead to proline auxotrophy, a dependence on exogenous proline to meet physiological demand. Proline auxotrophy is argued against by the finding that circulating proline levels are not different in HLD10 patients or mice (Table 1, Meng *et al.* 2017; Escande-Beillard *et al.* 2020). In addition, cultured wild-type and $Pycr2^{-/-}$ neuronal stem cells expanded equivalently in proline-free medium (Escande-Beillard *et al.* 2020). However, when $Pycr2^{-/-}$ mice were placed on a proline-free synthetic diet, they gained even less weight, whereas wild-type mice were unaffected (Figure 5). This would seem to indicate that normal levels of dietary proline at least partially suppress some aspects of the phenotype in these mice, though whether these include neurodevelopmental phenotypes relevant to HLD10 is unclear. Furthermore, in humans, the CL phenotype associated with *PYCR1* mutations is most logically associated with the demand for the proline-rich protein elastin in the affected tissues. This is most directly supported by mutations in elastin (*ELN*) itself and functionally related proteins such as fibulins also causing CL. The role for proline biosynthesis as central to the pathogenesis is also supported by mutations in P5CS (*ALDH18A1*) causing CL. Mouse elastin has 94 prolines of 860 total (10.93%), while human elastin has 100 prolines out of 786 total (12.72%; transcript 205, encoding the longest protein isoform). Thus, human elastin is more proline-rich, but one would say that mouse elastin is also proline-rich. The shear bulk of elastin required in skin and other organs in humans may contribute to proline becoming limiting more rapidly if demand does not scale in linear proportion to size, and this may account for why $Pycr1^{-/-}$ mice do not have a clear cutis laxa phenotype.

The human genetics of *ALDH18A1/P5CS* are also interesting. Recessive mutations cause autosomal recessive CL type 3 A (OMIM# 219150) (Baumgartner *et al.* 2000), but some alleles, such as homozygous H784Y mutations, do not impair activity or proline synthesis (Bicknell *et al.* 2008). In addition, dominant mutations in *ALDH18A1* cause spastic paraplegia 9 (Coutelier *et al.* 2015), all are point mutations and possibly act through a dominant negative activity (Panza *et al.* 2016). As P5CS produces the common precursor substrate for both PYCR1 and -2, one might anticipate that the phenotype of *ALDH18A1* mutations would look like the combined HLD10/CL disease. While there are cognitive issues in some *ALDH18A1/CL* patients, the SPG9 patients did not have cutaneous abnormalities (Coutelier *et al.* 2015). Given these still unexplained disparities, it is worth considering whether a failure to synthesize proline from P5C is the critical defect in *PYCR1* and -2 mutations. The lack of change in circulating proline levels or its precursors in our $Pycr2^{-/-}$ mice or in primary fibroblast cultures from those mice could suggest that decreased proline levels are indeed not the central disease mechanism, unless the demand for proline in translation is driven by more cell-intrinsic mechanisms and not by systemic levels. Our finding that dietary proline levels influence the severity of the $Pycr2$ phenotype argues that this is not entirely the case, and exogenously supplied proline is available and able to at least partially offset the lack of synthesis. In addition, *Aldh18a1*-null mice, generated through the KOMP program, die before 14-days-of-age, consistent with the severe phenotype of *Pycr1/Pycr2* double mutants (https://www.mousephenotype.org/data/genes/MGI:1888908). Other mechanisms such as increased cerebral glycine due to elevated SHMT2 levels are likely to also contribute to the pathophysiology of HLD10 (Escande-Beillard *et al.* 2020). However, without additional *in vivo* studies, it seems premature to discount the possibility that proline auxotrophy could also contribute to some aspects of HLD10, and perhaps even more to CL.

The *Pycr1* and *Pycr2* genes in mice are also clearly partially redundant with one another. The ability of these genes to compensate for one another was called into question by the observation that when one is lost in the brain, the expression of the other is

also severely reduced (Escande-Beillard *et al.* 2020). However, when both genes are completely absent in mice, the phenotype is much greater than additive, with only two surviving mice recovered and these were severely runted and unhealthy (Figure 5). Thus, through the classical genetic approach of making the double mutant, we found that these genes are indeed partially redundant ("partially" because the *Pycr2*$^{-/-}$ mice do have a phenotype). This is also consistent with our yeast complementation studies (Figure 4). The reported lack of compensation may be specific to the nervous system, and we do not know what caused the lethality in double mutant mice, but neurological phenotypes are rarely embryonic lethal. The proteins are in close proximity in mitochondria (Escande-Beillard *et al.* 2020), and the reduced levels of PYCR1 in the absence of PYCR2 may reflect protein instability and not gene expression. If protein instability issues could be overcome by increased gene expression, a better understanding of the gene regulatory features controlling expression may suggest new therapeutic strategies to upregulate *PYCR1* in the nervous system in *HLD10* patients and *PYCR2* in the tissues relevant to CL.

In addition to CL and HLD10, proline metabolism also plays important roles in many types of cancer, and *PYCR1* is a known oncogene that is frequently upregulated in cancer (Tanner *et al.* 2018; Burke *et al.* 2020; D'Aniello *et al.* 2020; Huynh *et al.* 2020). The most straightforward contribution of PYCRs is that they increase the availability of proline, but the role of proline metabolism in cancer has much broader and more varied implications. For example, during oncogenesis, cells must rewire their metabolic pathways to enable the high levels of proliferation and migration seen in cancer, and the metabolism of nonessential amino acids, including proline, is central to this process (Liu *et al.* 2015; Geck and Toker 2016; Choi and Coloff 2019). In addition, extracellular matrix proteins such as collagen are rich in proline, and can be both a source of this amino acid due to the matrix metalloproteinases released by cancer cells (Page-McCaw *et al.* 2007), and play a role in cancer progression by influencing the transition to a mesenchymal state and metastasis (Burke *et al.* 2020; D'Aniello *et al.* 2020). Proline metabolism may also be important in managing the increased production of reactive oxygen species in cancer, both via the metabolic pathway (Hollinshead *et al.* 2018; Schworer *et al.* 2020) and potentially via intrinsic antioxidant capabilities of proline itself (Burke *et al.* 2020). Finally, a corollary benefit of the additional proline from PYCR1 upregulation is that it would help to avoid activation of the integrated stress response, which results in global translation repression, by the presence of uncharged prolyl-tRNAs and/or ribosome stalling caused by the lack of charged prolyl-tRNA (Burke *et al.* 2020; D'Aniello *et al.* 2020).

As animal models of human disease, the *Pycr1*$^{-/-}$ mice are disappointing, and some co-manipulation of *Pycr2* or exogenous proline deprivation may be required to produce a CL-relevant phenotype. The *Pycr2*$^{-/-}$ mice are more promising as a model of HLD10, although their phenotype is still milder than the human disease, and onset is in early adulthood, in contrast to the congenital disease in humans. In *Xenopus, Pycr1* knock-down morphants were used, and showed epidermal hypoplasia due to apoptosis with ectodermal edema, together with a loss of red blood cells (Reversade *et al.* 2009). These results suggested that *Pycr1* plays a role in both skin and blood cell development, and that *Xenopus* may provide a valid experimental system. Similarly, zebrafish with a knockdown of *pycr1b* show some features of HLD10, including microcephaly, whereas knockdown of *pycr1a* causes a skin phenotype (Reversade *et al.* 2009; Nakayama *et al.* 2015; Liang *et al.* 2019). Our results indicate that yeast may also provide a model system, particularly given the ability of the human genes to complement the loss of yeast *PRO3*. At the very least, this yeast assay likely provides a screen for the potential pathogenicity of human variants of unknown significance.

Conclusions

In this study, we have expanded the phenotypic description of *Pycr2*$^{-/-}$ mice, demonstrated through analysis of *Pycr1/Pycr2* double-mutant mice that these genes are functionally redundant, and demonstrated through use of a proline-free diet that proline auxotrophy contributes to at least some aspects of the *Pycr2*$^{-/-}$ phenotype. These findings will help in future studies to optimize the disease-relevance of these mouse models, and also in understanding the complex pathophysiology and genetics of cutis laxa and hypomyelinating leukodystrophy.

Data Availability

The authors affirm that all data necessary for confirming the conclusions of this article are present within the article, figures, and tables. All materials and reagents are available from investigators upon request. Supplemental Material available at figshare: https://doi.org/10.25386/genetics.14204303.

Conflicts of interest

The authors declare no conflicts of interest. Dr. Stum is currently an employee of ClearH2O, but all data included in this paper were generate prior to her employment.

Ethics approval

All animal studies were approved by the Animal Care and Use Committee of The Jackson Laboratory under protocol number 1026.

Literature cited

Barbaric I, Wells S, Russ A, Dear TN. 2007. Spectrum of ENU-induced mutations in phenotype-driven and gene-driven screens in the mouse. Environ Mol Mutagen 48:124–142.

Baumgartner MR, Hu CA, Almashanu S, Steel G, Obie C, *et al.* 2000. Hyperammonemia with reduced ornithine, citrulline, arginine and proline: a new inborn error caused by a mutation in the gene encoding delta(1)-pyrroline-5-carboxylate synthase. Hum Mol Genet. 9:2853–2858.

Bicknell LS, Pitt J, Aftimos S, Ramadas R, Maw MA, *et al.* 2008. A missense mutation in ALDH18A1, encoding Delta1-pyrroline-5-carboxylate synthase (P5CS), causes an autosomal recessive neurocutaneous syndrome. Eur J Hum Genet. 16: 1176–1186.,

Burke L, Guterman I, Palacios Gallego R, Britton RG, Burschowsky D, *et al.* 2020. The Janus-like role of proline metabolism in cancer. Cell Death Discov. 6:104.,

Chase HB. 1955. The physiology and histochemistry of hair growth. J Soc Cosmetic Chem. 6:9–14.

Chen Q, Park HC, Goligorsky MS, Chander P, Fischer SM, *et al.* 2012. Untargeted plasma metabolite profiling reveals the broad systemic consequences of xanthine oxidoreductase inactivation in mice. PLoS ONE 7:e37149.

Choi BH, Coloff JL. 2019. The diverse functions of non-essential amino acids in cancer. Cancers (Basel) 11:675.

Coutelier M, Goizet C, Durr A, Habarou F, Morais S, *et al.* 2015. Alteration of ornithine metabolism leads to dominant and recessive hereditary spastic paraplegia. Brain 138:2191–2205.

D'Aniello C, Patriarca EJ, Phang JM, Minchiotti G. 2020. Proline metabolism in tumor growth and metastatic progression. Front Oncol. 10:776.

Dasouki M, Markova D, Garola R, Sasaki T, Charbonneau NL, *et al.* 2007. Compound heterozygous mutations in fibulin-4 causing neonatal lethal pulmonary artery occlusion, aortic aneurysm, arachnodactyly, and mild cutis laxa. Am J Med Genet A 143A: 2635–2641.

De Ingeniis J, Ratnikov B, Richardson AD, Scott DA, Aza-Blanc P, *et al.* 2012. Functional specialization in proline biosynthesis of melanoma. PLoS ONE 7:e45190.

Dickinson ME, Flenniken AM, Ji X, Teboul L, Wong MD, *et al.* 2016. High-throughput discovery of novel developmental phenotypes. Nature 537:508–514.

Dimopoulou A, Fischer B, Gardeitchik T, Schroter P, Kayserili H, *et al.* 2013. Genotype-phenotype spectrum of PYCR1-related autosomal recessive cutis laxa. Mol Genet Metab. 110:352–361.

Escande-Beillard N, Loh A, Saleem SN, Kanata K, Hashimoto Y, *et al.* 2020. Loss of PYCR2 causes neurodegeneration by increasing cerebral glycine levels via SHMT2. Neuron 107:82–94.e86.

Geck RC, Toker A. 2016. Nonessential amino acid metabolism in breast cancer. Adv Biol Regul. 62:11–17.

Guernsey DL, Jiang H, Evans SC, Ferguson M, Matsuoka M, *et al.* 2009. Mutation in pyrroline-5-carboxylate reductase 1 gene in families with cutis laxa type 2. Am J Hum Genet. 85:120–129.

Hollinshead KER, Munford H, Eales KL, Bardella C, Li C, *et al.* 2018. Oncogenic IDH1 mutations promote enhanced proline synthesis through PYCR1 to support the maintenance of mitochondrial redox homeostasis. Cell Rep. 22:3107–3114.

Hoyer J, Kraus C, Hammersen G, Geppert JP, Rauch A. 2009. Lethal cutis laxa with contractural arachnodactyly, overgrowth and soft tissue bleeding due to a novel homozygous fibulin-4 gene mutation. Clin Genet. 76:276–281.

Hucthagowder V, Sausgruber N, Kim KH, Angle B, Marmorstein LY, *et al.* 2006. Fibulin-4: a novel gene for an autosomal recessive cutis laxa syndrome. Am J Hum Genet. 78:1075–1080.

Huynh TYL, Zareba I, Baszanowska W, Lewoniewska S, Palka J. 2020. Understanding the role of key amino acids in regulation of proline dehydrogenase/proline oxidase (prodh/pox)-dependent apoptosis/autophagy as an approach to targeted cancer therapy. Mol Cell Biochem. 466:35–44.

King LE, Jr., McElwee KJ, Sundberg JP. 2008. Alopecia areata. Curr Dir Autoimmun. 10:280–312.

Kouwenberg D, Gardeitchik T, Wevers RA, Haberle J, Morava E. 2011. Recognizable phenotype with common occurrence of microcephaly, psychomotor retardation, but no spontaneous bone fractures in autosomal recessive cutis laxa type IIB due to PYCR1 mutations. Am J Med Genet A 155A:2331–2332. author reply 2333–2334.

Kretz R, Bozorgmehr B, Kariminejad MH, Rohrbach M, Hausser I, *et al.* 2011. Defect in proline synthesis: pyrroline-5-carboxylate reductase 1 deficiency leads to a complex clinical phenotype with collagen and elastin abnormalities. J Inherit Metab Dis. 34: 731–739.

Liang ST, Audira G, Juniardi S, Chen JR, Lai YH, *et al.* 2019. Zebrafish carrying pycr1 gene deficiency display aging and multiple behavioral abnormalities. Cells 8:453.

Lin DS, Chang JH, Liu HL, Wei CH, Yeung CY, *et al.* 2011a. Compound heterozygous mutations in PYCR1 further expand the phenotypic spectrum of De Barsy syndrome. Am J Med Genet A 155A: 3095–3099.

Lin DS, Yeung CY, Liu HL, Ho CS, Shu CH, *et al.* 2011b. A novel mutation in PYCR1 causes an autosomal recessive cutis laxa with premature aging features in a family. Am J Med Genet A 155A: 1285–1289.

Liu W, Hancock CN, Fischer JW, Harman M, Phang JM. 2015. Proline biosynthesis augments tumor cell growth and aerobic glycolysis: involvement of pyridine nucleotides. Sci Rep. 5:17206.

Loeys B, Van Maldergem L, Mortier G, Coucke P, Gerniers S, *et al.* 2002. Homozygosity for a missense mutation in fibulin-5 (FBLN5) results in a severe form of cutis laxa. Hum Mol Genet. 11: 2113–2118.

Markova D, Zou Y, Ringpfeil F, Sasaki T, Kostka G, *et al.* 2003. Genetic heterogeneity of cutis laxa: a heterozygous tandem duplication within the fibulin-5 (FBLN5) gene. Am J Hum Genet. 72:998–1004.

McElwee KJ, Boggess D, Miller J, King LE, Jr., Sundberg JP. 1999. Spontaneous alopecia areata-like hair loss in one congenic and seven inbred laboratory mouse strains. J Investig Dermatol Symp Proc. 4:202–206.

Meng L, Donti T, Xia F, Niu Z, Al Shamsi A, *et al.* 2017. Homozygous variants in pyrroline-5-carboxylate reductase 2 (PYCR2) in patients with progressive microcephaly and hypomyelinating leukodystrophy. Am J Med Genet A 173:460–470.

Morava E, Guillard M, Lefeber DJ, Wevers RA. 2009. Autosomal recessive cutis laxa syndrome revisited. Eur J Hum Genet. 17: 1099–1110.

Nakayama T, Al-Maawali A, El-Quessny M, Rajab A, Khalil S, *et al.* 2015. Mutations in PYCR2, encoding pyrroline-5-carboxylate reductase 2, cause microcephaly and hypomyelination. Am J Hum Genet. 96:709–719.

Nouri N, Aryani O, Nouri N, Kamalidehghan B, Houshmand M. 2013. Cutis laxa Type II with mutation in the pyrroline-5-carboxylate reductase 1 gene. Pediatr Dermatol. 30:e265–e267.

Occhi S, Zambroni D, Del Carro U, Amadio S, Sirkowski EE, *et al.* 2005. Both laminin and Schwann cell dystroglycan are necessary for proper clustering of sodium channels at nodes of ranvier. J Neurosci. 25:9418–9427.

Page-McCaw A, Ewald AJ, Werb Z. 2007. Matrix metalloproteinases and the regulation of tissue remodelling. Nat Rev Mol Cell Biol. 8: 221–233.

Panza E, Escamilla-Honrubia JM, Marco-Marin C, Gougeard N, De Michele G, *et al.* 2016. ALDH18A1 gene mutations cause dominant spastic paraplegia SPG9: loss of function effect and plausibility of a dominant negative mechanism. Brain 139:e3.

Reeds PJ. 2000. Dispensable and indispensable amino acids for humans. J Nutr. 130:1835S–1840S.

Renard M, Holm T, Veith R, Callewaert BL, Ades LC, *et al.* 2010. Altered TGFbeta signaling and cardiovascular manifestations in patients with autosomal recessive cutis laxa type I caused by fibulin-4 deficiency. Eur J Hum Genet. 18:895–901.

Reversade B, Escande-Beillard N, Dimopoulou A, Fischer B, Chng SC, *et al.* 2009. Mutations in PYCR1 cause cutis laxa with progeroid features. Nat Genet. 41:1016–1021.

Ritelli M, Palit A, Giacopuzzi E, Inamadar AC, Dordoni C, *et al.* 2017. Clinical and molecular characterization of a 13-year-old Indian boy with cutis laxa type 2B: identification of two novel PYCR1 mutations by amplicon-based semiconductor exome sequencing. J Dermatol Sci. 88:141–143.

Scherrer DZ, Baptista MB, Matos AH, Maurer-Morelli CV, Steiner CE. 2013. Mutations in PYCR1 gene in three families with autosomal recessive cutis laxa, type 2. Eur J Med Genet. 56:336–339.

Schworer S, Berisa M, Violante S, Qin W, Zhu J, *et al.* 2020. Proline biosynthesis is a vent for TGFbeta-induced mitochondrial redox stress. EMBO J. 39:e103334.

Skidmore DL, Chitayat D, Morgan T, Hinek A, Fischer B, *et al.* 2011. Further expansion of the phenotypic spectrum associated with mutations in ALDH18A1, encoding Delta(1)-pyrroline-5-carboxylate synthase (P5CS). Am J Med Genet A 155A:1848–1856.

Sundberg JP, Cordy WR, King LE. Jr., 1994. Alopecia areata in aging C3H/HeJ mice. J Invest Dermatol. 102:847–856.

Sundberg JP, Silva KA. 2012. What color is the skin of a mouse? Vet Pathol. 49:142–145.

Szabo Z, Levi-Minzi SA, Christiano AM, Struminger C, Stoneking M, *et al.* 1999. Sequential loss of two neighboring exons of the tropoelastin gene during primate evolution. J Mol Evol. 49:664–671.

Tanner JJ, Fendt SM, Becker DF. 2018. The proline cycle as a potential cancer therapy target. Biochemistry 57:3433–3444.

Tassabehji M, Metcalfe K, Hurst J, Ashcroft GS, Kielty C, *et al.* 1998. An elastin gene mutation producing abnormal tropoelastin and abnormal elastic fibres in a patient with autosomal dominant cutis laxa. Hum Mol Genet. 7:1021–1028.

Urban Z, Gao J, Pope FM, Davis EC. 2005. Autosomal dominant cutis laxa with severe lung disease: synthesis and matrix deposition of mutant tropoelastin. J Invest Dermatol. 124:1193–1199.

Wooley CM, Sher RB, Kale A, Frankel WN, Cox GA, *et al.* 2005. Gait analysis detects early changes in transgenic SOD1(G93A) mice. Muscle Nerve 32:43–50.

Wooley CM, Xing S, Burgess RW, Cox GA, Seburn KL. 2009. Age, experience and genetic background influence treadmill walking in mice. Physiol Behav. 96:350–361.

Yildirim Y, Tolun A, Tuysuz B. 2011. The phenotype caused by PYCR1 mutations corresponds to geroderma osteodysplasticum rather than autosomal recessive cutis laxa type 2. Am J Med Genet A 155A:134–140.

Zaki MS, Bhat G, Sultan T, Issa M, Jung HJ, *et al.* 2016. PYCR2 Mutations cause a lethal syndrome of microcephaly and failure to thrive. Ann Neurol. 80:59–70.

Zampatti S, Castori M, Fischer B, Ferrari P, Garavelli L, *et al.* 2012. De Barsy Syndrome: a genetically heterogeneous autosomal recessive cutis laxa syndrome related to P5CS and PYCR1 dysfunction. Am J Med Genet A 158A:927–931.

Zhang MC, He L, Giro M, Yong SL, Tiller GE, *et al.* 1999. Cutis laxa arising from frameshift mutations in exon 30 of the elastin gene (ELN). J Biol Chem. 274:981–986.

Communicating editor: J. Flint